

## Supplementary information

### 1 Materials characterization

The crystal structures of the products were determined using X-ray diffraction (XRD, Ultima IV-185, Japan) and confocal laser microraman spectrometer (Raman, Horiba LabRAM HR Evolution, Japan). The elemental valence state of the compositions was analyzed by X-ray photoelectron spectroscopy (XPS, Thermo KAlpha, USA). Surface area and pore size distribution of the product are measured by Brunauer Emmett Teller (BET) (Quantachrome Autosorb IQ MP, USA). The products' morphological structures were examined using transmission electron microscopy (TEM, JEOL JEM-F200, Japan) and scanning electron microscopy (SEM, HITACHI SU8020, Japan).

### 2 Electrochemical measurements

The prepared electrode material, acetylene black, and polytetrafluoroethylene (PTFE) were mixed at a mass ratio of 7:2:1 to form a film with a thickness of about 0.1 mm, and dried at 60 °C for 5 h. The films were fixed to a nickel foam using a tablet press. The weight of active material is about 3.5 mg. Each electrode had a geometric surface area of about 2 cm<sup>2</sup>. The electrode material, activated carbon and HgO/Hg electrode were used as working electrode, counter electrode and reference electrode respectively. 6 mol/L KOH solution was used as electrolyte. The electrochemical tests were performed using a Chenhua CHI660E electrochemical workstation, and cycle stability testing was performed using an LAND CT3002A instrument.

The specific capacitance of the electrode material was calculated using Eq. (S1):

$$C_s = \frac{I \times \Delta t}{m \times \Delta V} \quad (\text{S1})$$

where  $C_s$  is the specific capacitance (F/g);  $I$  is the discharge current (A/g);  $\Delta t$  is the discharge time (s);  $m$  is the mass of the electrode material (g);  $\Delta V$  is the voltage difference (V).

The mass ratio of the positive and negative materials of the asymmetric capacitor was calculated using Eq. (S2) to ensure charge balance:

$$R = \frac{m_+}{m_-} = \frac{C_- \cdot \Delta V_-}{C_+ \cdot \Delta V_+} \quad (\text{S2})$$

where  $R$  is the ratio of the masses of the positive and negative electrodes;  $m_+$  and  $m_-$  are the load masses of the positive and negative electrodes, respectively, with the unit being g;  $C_+$  and  $C_-$  are the specific capacitance of the positive and negative electrodes calculated according to Eq. (S1), respectively;  $\Delta V_+$  and  $\Delta V_-$  are the test potential ranges of the positive and negative electrodes in the three-electrode system, respectively.

The following equation was employed to calculate the energy density ( $E$ ) and power density ( $P$ ) of the experimental ASCs:

$$E = \frac{C \times \Delta V^2}{7200} \quad (\text{S3})$$

$$P = \frac{E \times 3600}{\Delta t} \quad (\text{S4})$$

where  $E$  is the energy density (W·h/kg) and  $P$  is the power density (W/kg).

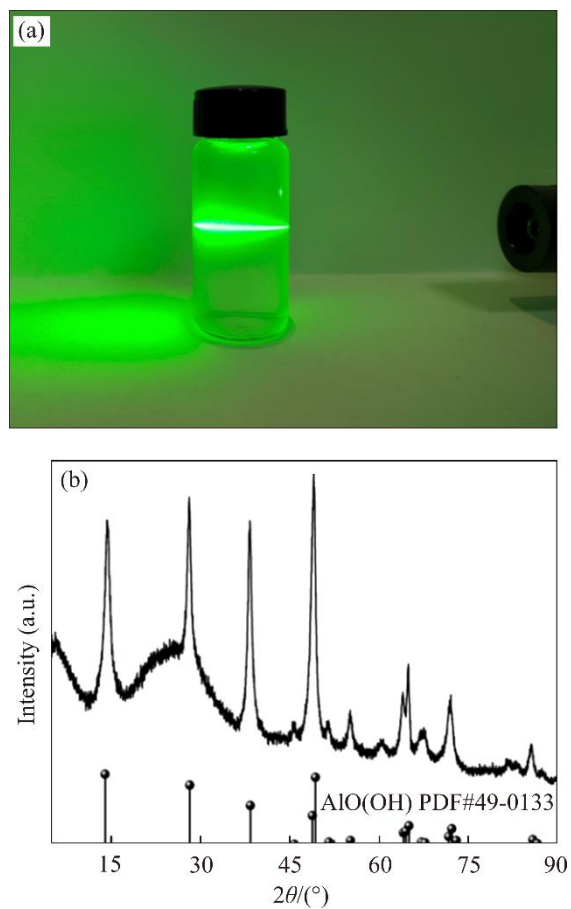


**Figure S1** 1 mmol  $\text{AlCl}_3 \cdot 6\text{H}_2\text{O}$  was dissolved in 40 mL deionized water and reacted at 180 °C for 7 h: (a) The supernatant after the reaction irradiated with a laser pointer to produce the Tyndall phenomenon; (b) XRD pattern of the product after hydrolysis of  $\text{AlCl}_3 \cdot 6\text{H}_2\text{O}$

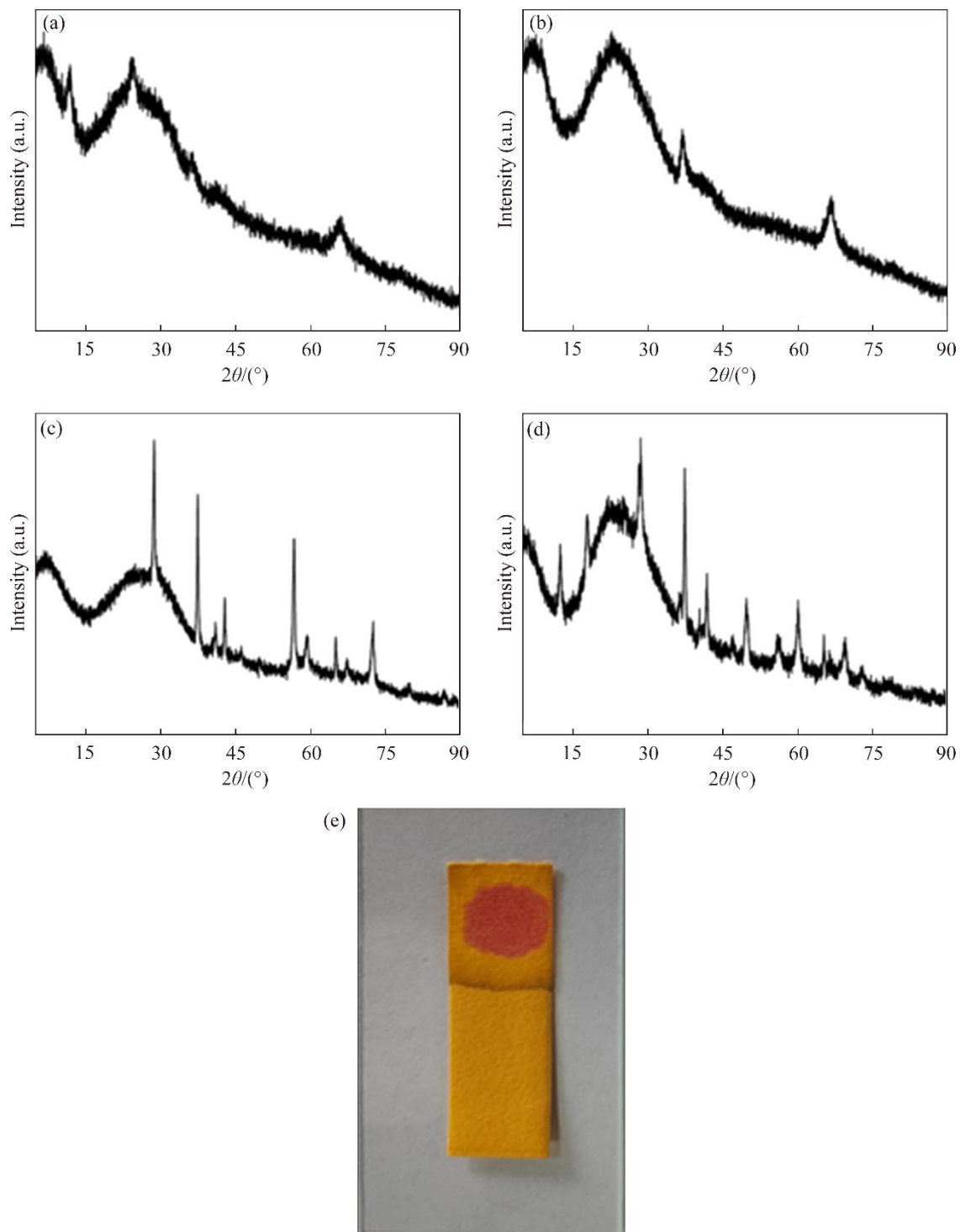


**Figure S2** XRD pattern of the product after hydrothermal reaction (a) 1.5 mmol  $\text{KMnO}_4$  dissolved in 40 mL deionized water; (b) 1.5 mmol  $\text{KMnO}_4$  and 1 mmol  $\text{AlCl}_3 \cdot 6\text{H}_2\text{O}$  dissolved in 40 mL of deionized water; (c) 1.5 mmol  $\text{KMnO}_4$ , 1.5 mmol  $\text{MnCl}_2 \cdot 4\text{H}_2\text{O}$  and a small amount of hydrochloric acid configured into 40 mL aqueous solution; (d) 1.5 mmol  $\text{KMnO}_4$ , 1.5 mmol  $\text{MnCl}_2 \cdot 4\text{H}_2\text{O}$  and 3 mmol  $\text{KCl}$  dissolved in 40 mL deionized water; (e) 1 mmol of  $\text{AlCl}_3 \cdot 6\text{H}_2\text{O}$  dissolved in 40 mL of deionized water. The supernatant after hydrothermal reaction was detected by pH paper, and the result showed acidity

**Table S1** Corresponding to Figure 2(d), binding energies of Mn 2p<sub>3/2</sub> and Mn 2p<sub>1/2</sub> orbitals in different samples eV

Sample	Mn 2p <sub>3/2</sub>	Mn 2p <sub>1/2</sub>
MnO <sub>2</sub>	641.7	653.55
MnO <sub>2</sub> -1	642.1	653.85
MnO <sub>2</sub> -3	642.0	653.65
MnO <sub>2</sub> -5	642.1	653.80

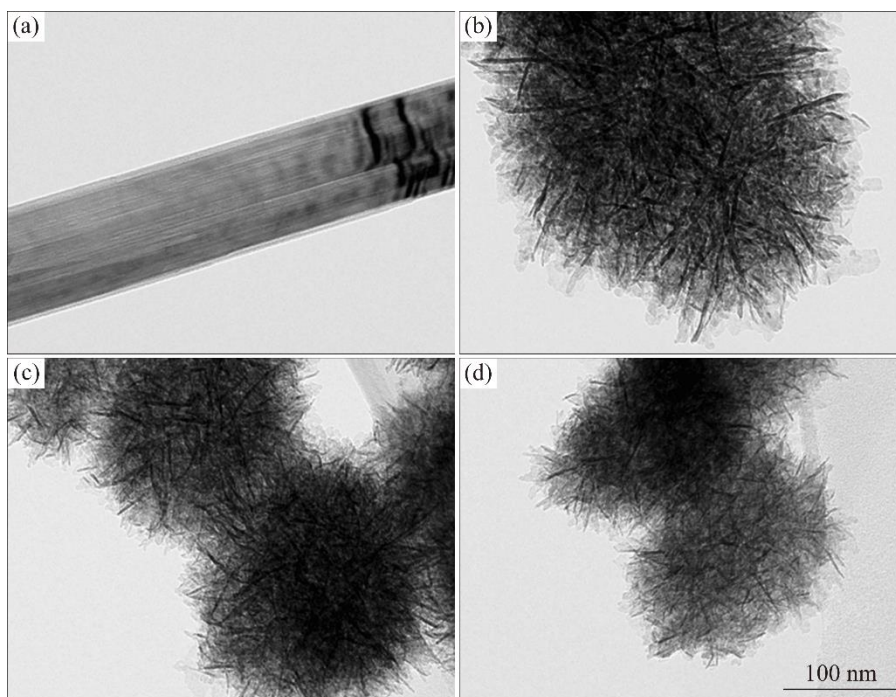


**Figure S3** TEM images: (a) MnO<sub>2</sub>; (b) MnO<sub>2</sub>-1; (c) MnO<sub>2</sub>-3; (d) MnO<sub>2</sub>-5

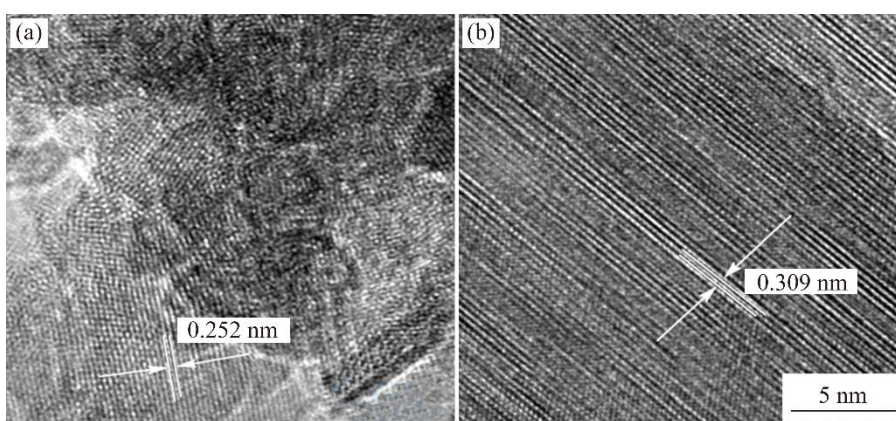


**Figure S4** HRTEM diagram of MnO<sub>2</sub>-1

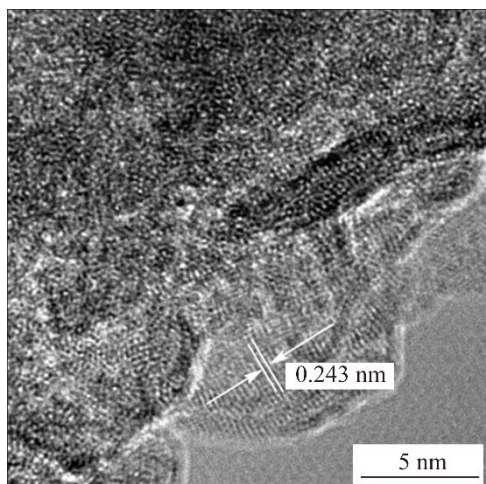


**Figure S5** HRTEM diagram of MnO<sub>2</sub>-5

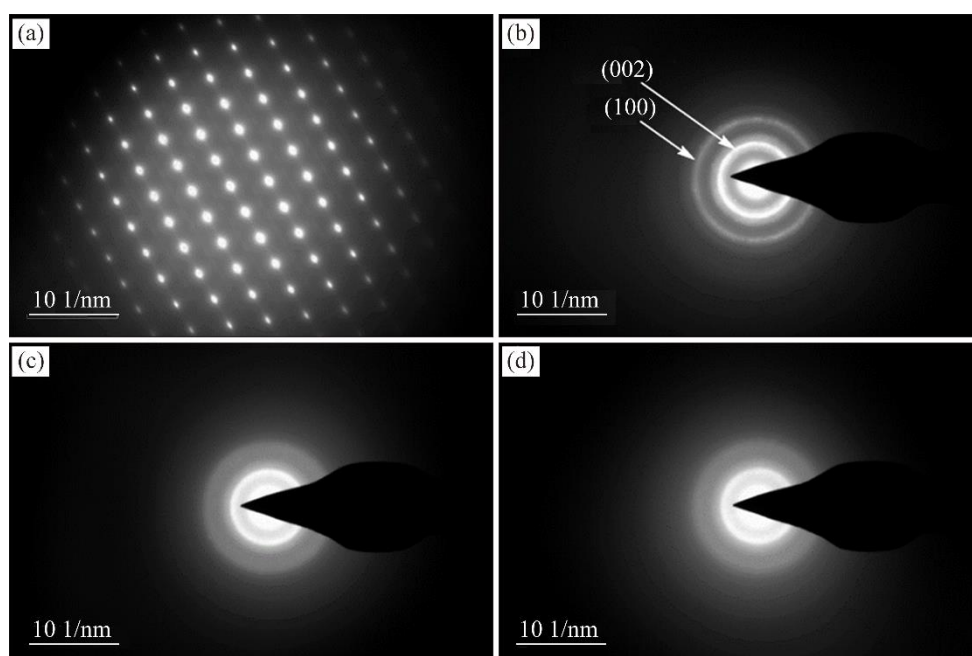


**Figure S6** SAED pattern: (a) MnO<sub>2</sub>; (b) MnO<sub>2</sub>-1; (c) MnO<sub>2</sub>-3; (d) MnO<sub>2</sub>-5

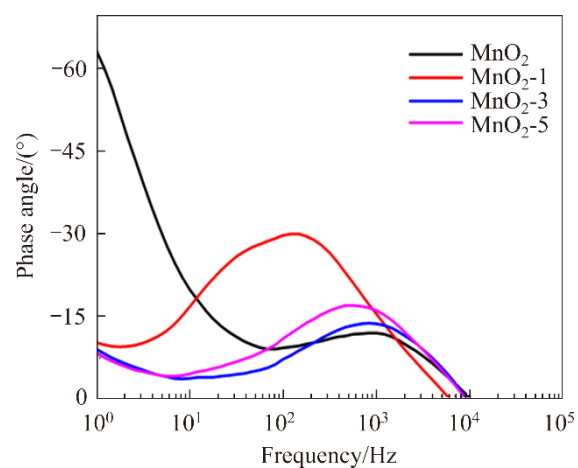


**Figure S7** Bode plots

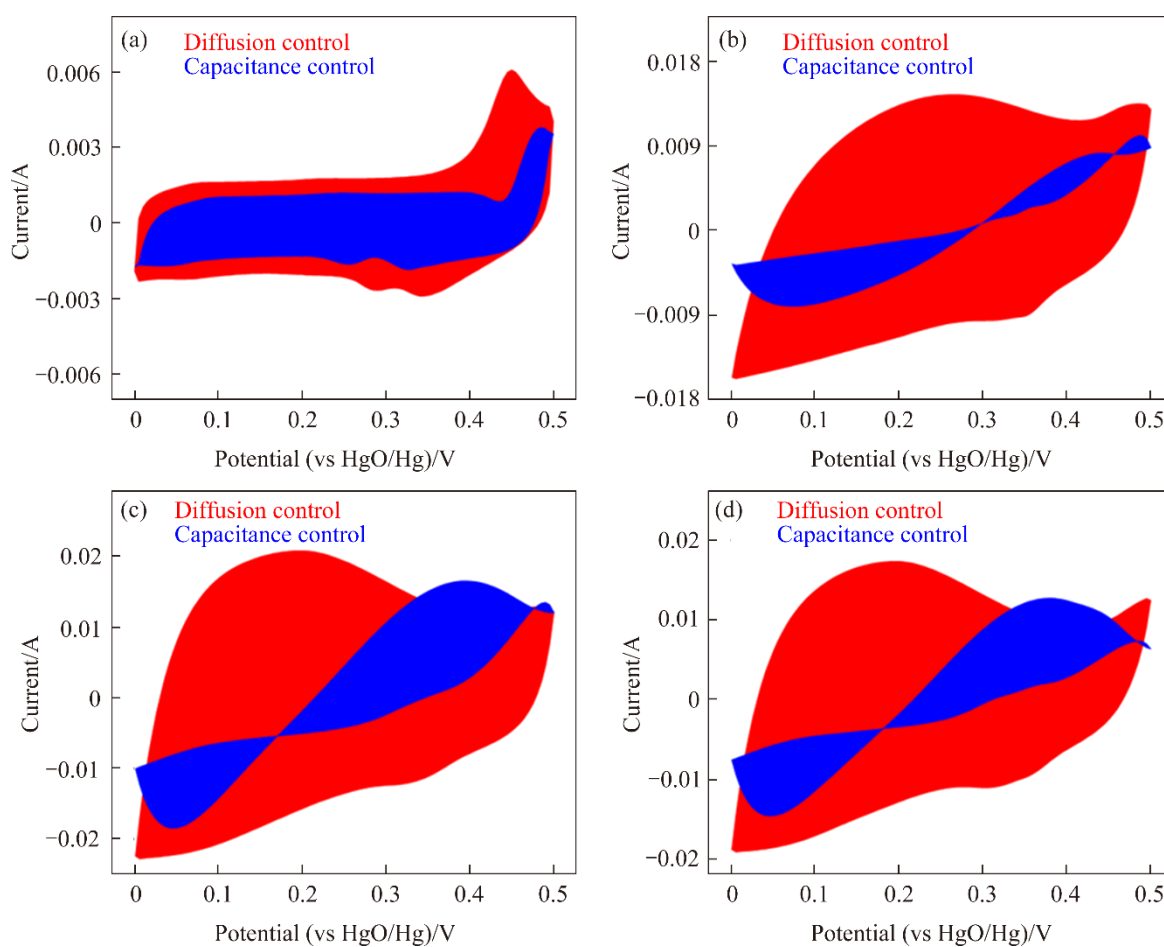


**Figure S8** Capacitance contribution plot for 20 mV/s: (a) MnO<sub>2</sub>; (b) MnO<sub>2</sub>-1; (c) MnO<sub>2</sub>-3; (d) MnO<sub>2</sub>-5

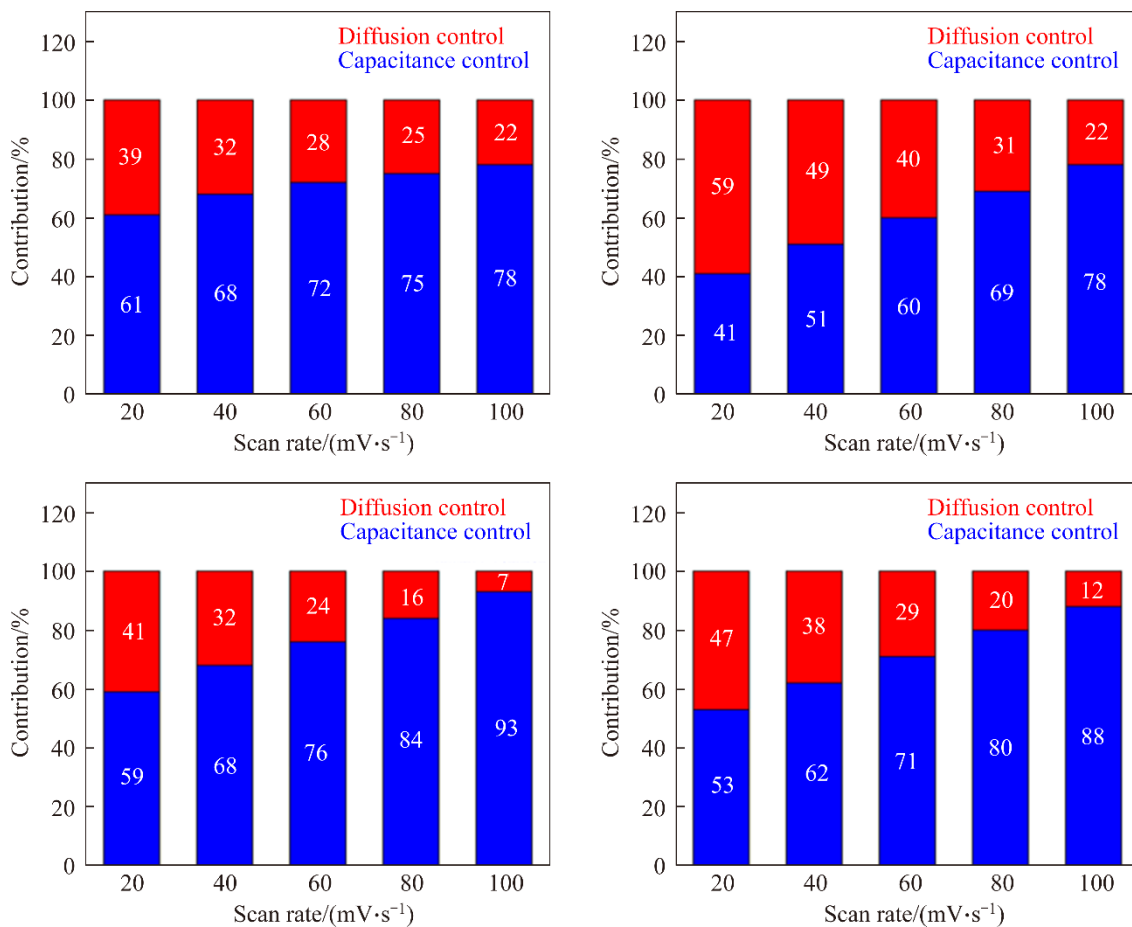


**Figure S9** Contribution rate of diffusion control process and capacitance control process for different electrodes at different scan rates: (a) MnO<sub>2</sub>; (b) MnO<sub>2</sub>-1; (c) MnO<sub>2</sub>-3; (d) MnO<sub>2</sub>-5

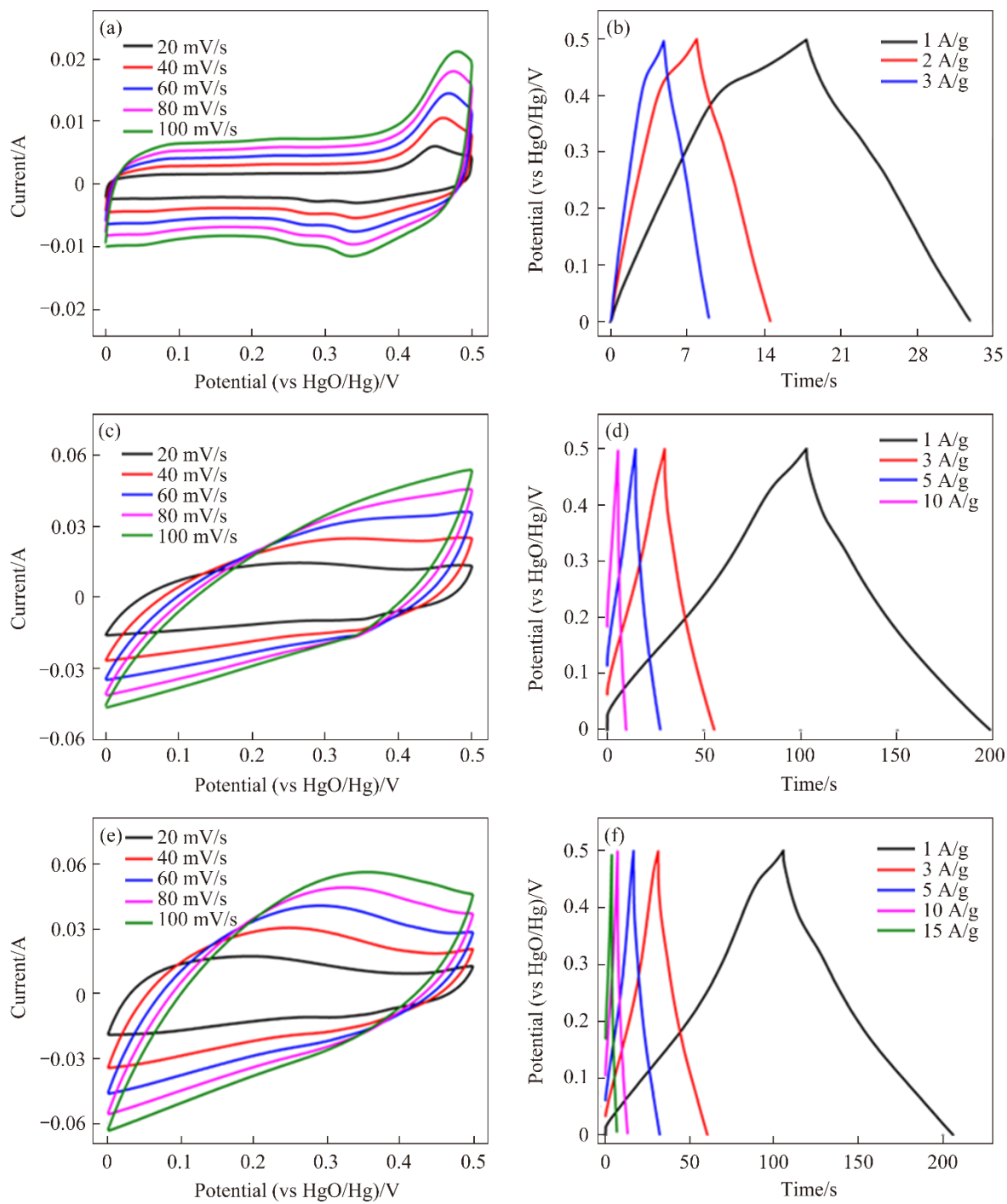


**Figure S10** (a, c, e) CV curves and (b, d, f) GCD curves of MnO<sub>2</sub> (a, b), MnO<sub>2</sub>-1 (c, d), and MnO<sub>2</sub>-5 (e, f)

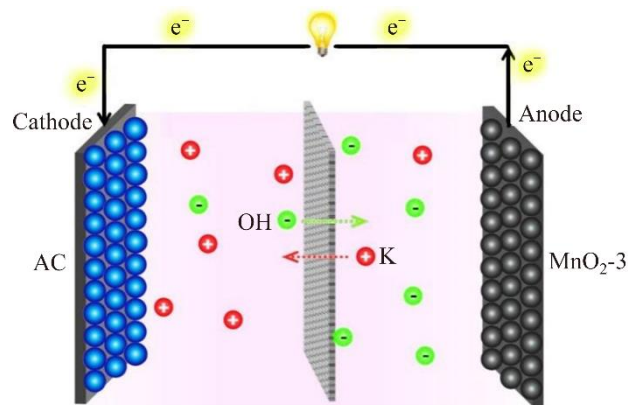


**Figure S11** Internal structure of asymmetric supercapacitor

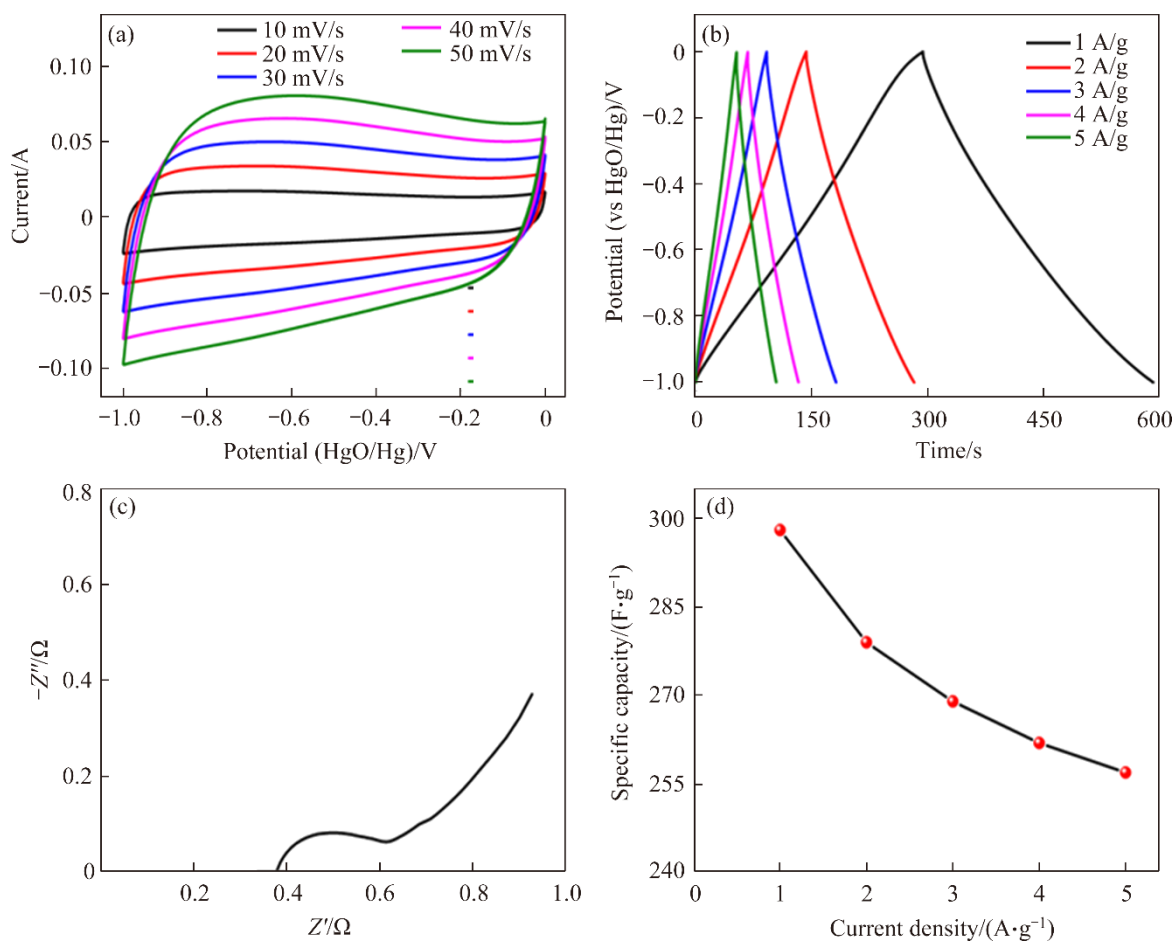


**Figure S12** AC (YEC-8A) was purchased from Fuzhou Yihuan Carbon Co., Ltd., China. Electrochemical performance of activated carbon: (a) CV curve, (b) GCD curve, (c) Nyquist plot of EIS, (d) Specific capacitance at different current densities. It can be seen from Figure S12(a) that all CV curves are rectangular, and there is no redox peak, showing the characteristics of a typical electric double layer capacitor. As shown in (b), all GCD curves are almost symmetrical at different current densities, confirming that AC has good reversibility. (c) is the EIS spectra of AC, the low equivalent series resistance reflects the easy transmission of electrons. The specific capacitance of AC at 1 A/g is 298 F/g

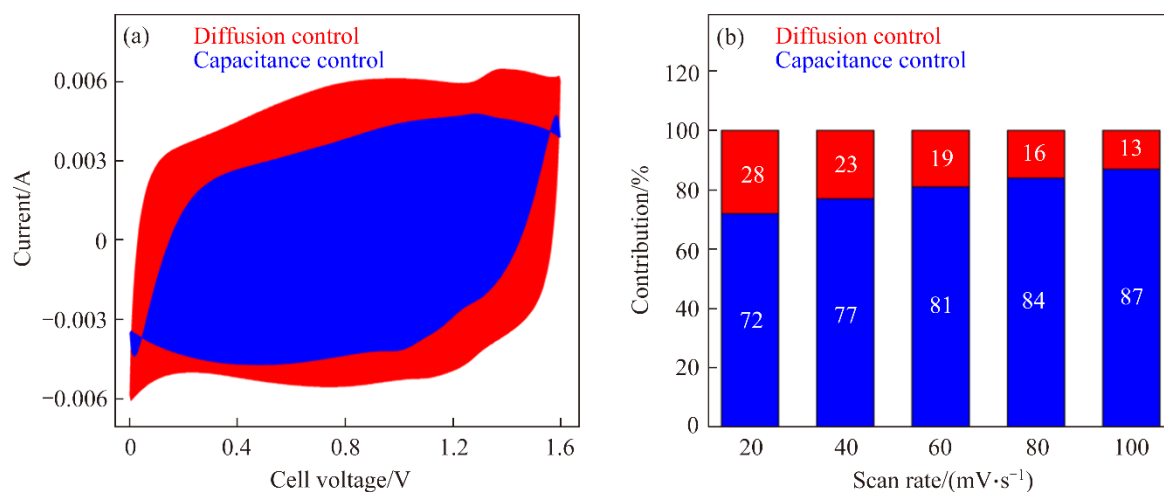


**Figure S13** ASC: (a) Capacitance contribution plot for 20 mV/s; (b) Capacitance contribution of diffusion control process and capacitance control process

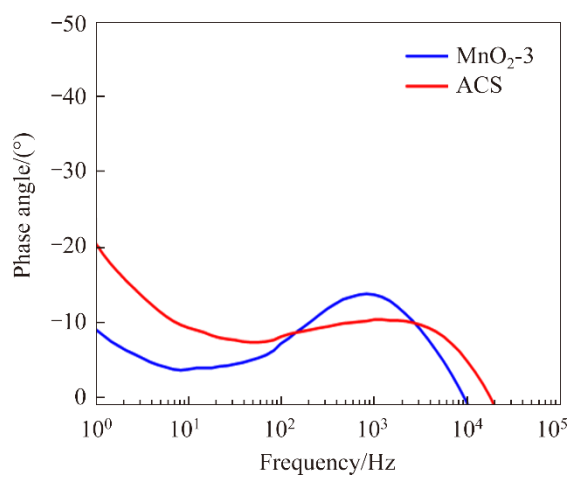


**Figure S14** Relationship between phase angle and frequency of MnO<sub>2</sub>-3 and ACS

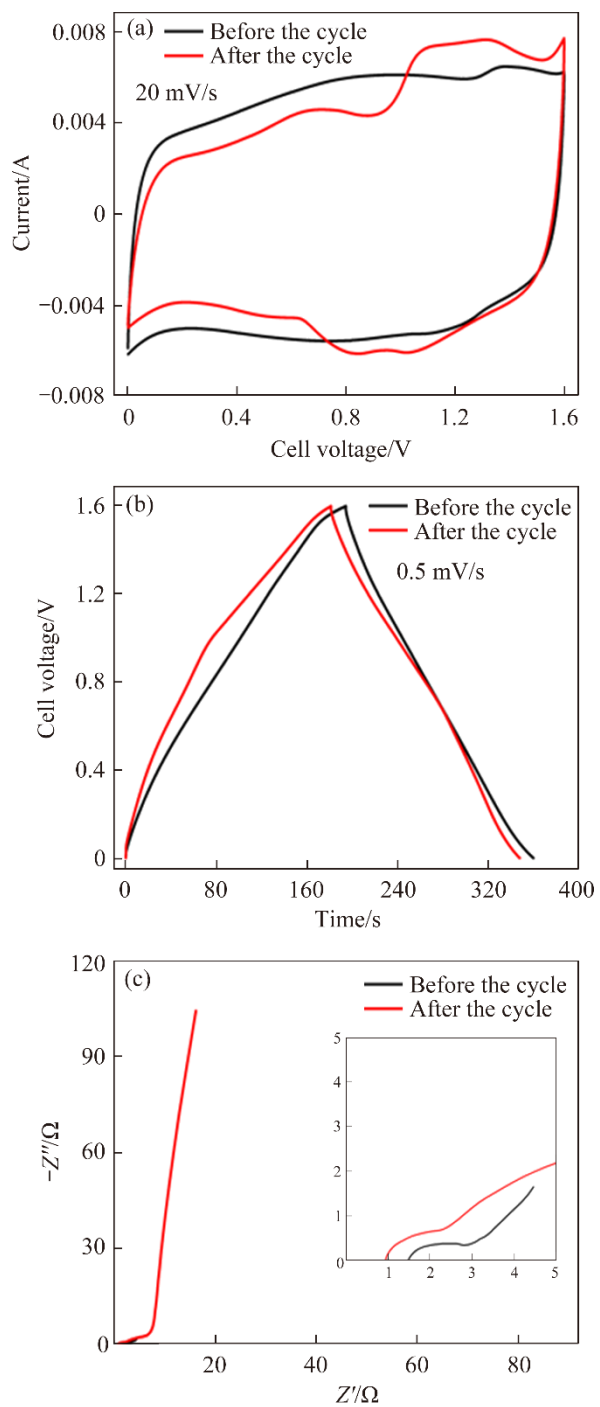


**Figure S15** Electrochemical tests of ASC before and after cycling: (a) CV curve; (b) GCD curve; (c) EIS curve

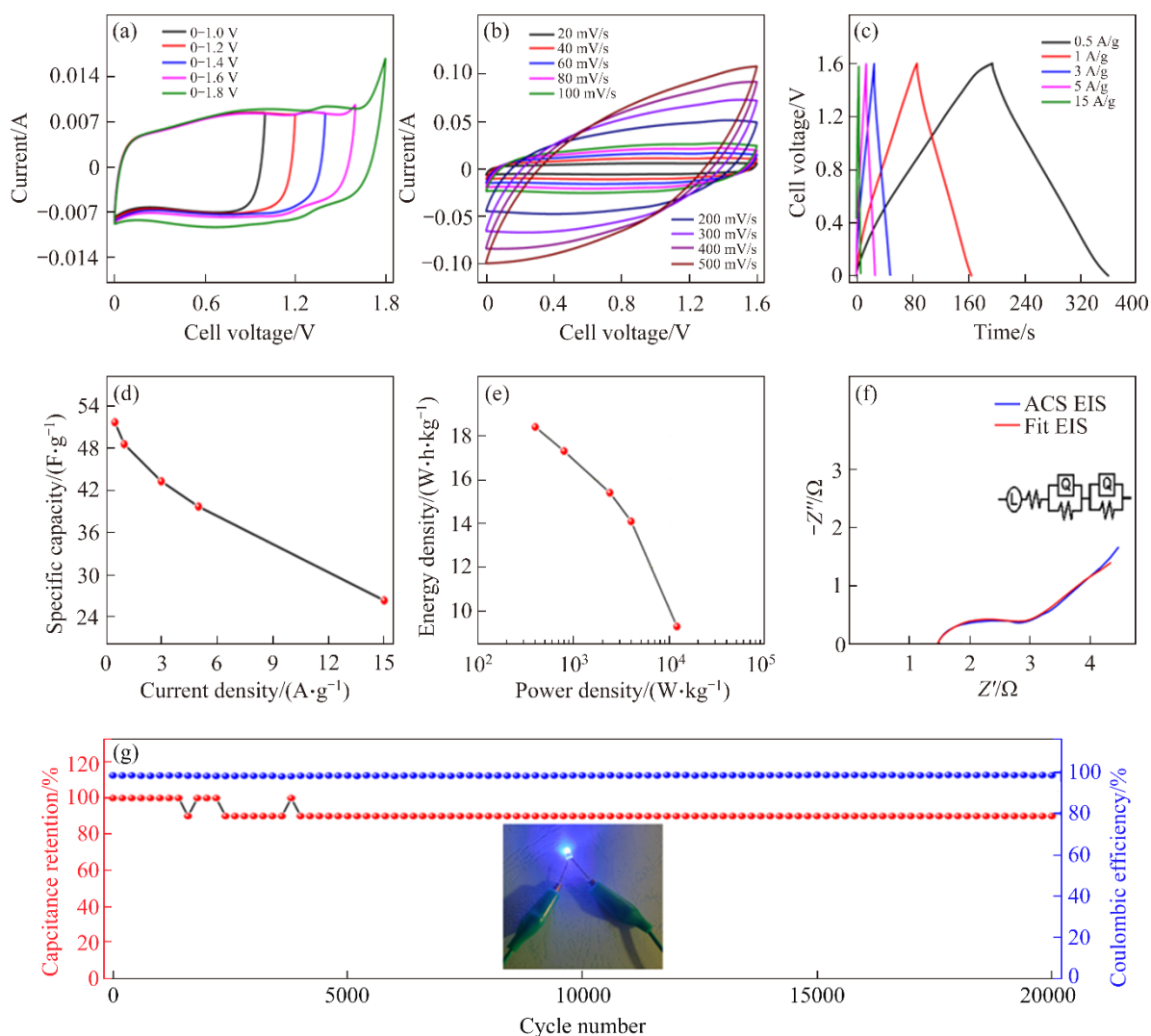


**Figure S16** MnO<sub>2</sub>-3//AC-ASC: (a) CV curve in different voltage range; (b) CV curve with different scan rate; (c) GCD curve; (d) Relationship between current density and specific capacity; (e) Relationship between power density and energy density; (f) EIS spectrum; (g) Cycle stability and coulomb efficiency of 3 A/g, the illustration is that two ASCs in series can drive the LED lamp

In order to evaluate the practical application performance of MnO<sub>2</sub>-3, MnO<sub>2</sub>-3 is used as the cathode material and AC is used as the anode material to assemble an ASC. Figure S11 shows the detailed assembly structure. Since the electrolyte of ASC is an aqueous solution, higher voltage will cause water decomposition, so ASC needs a stable voltage range. Figure S16(a) shows CV curves of ASC in different voltage windows. When the voltage reaches 1.8 V, ASC begins to appear water decomposition, so 0–1.6 V is the stable working voltage of ASC. Figure S16(b) shows CV curves of ASC at different scanning rates. Even at 500 mV/s, the shape of the CV curve remains unchanged, showing excellent rate capability. Figure S16(c) shows that the GCD curve of ASC is approximately isosceles triangle, which means that it has good capacitance characteristics. Figure S16(d) summarizes the specific capacitance of ASC at different current densities. The specific capacitance at 0.5 A/g is 51.7 F/g. When the current density is increased by 10 times (5 A/g), the specific capacitance can still be maintained at 39.7 F/g, indicating that ASC has excellent rate performance. Figure S16(e) summarizes the relationship between energy density and power density of ASC. It can be seen from the figure that the energy density is as high as 18.4 W·h/kg at the power density of 400 W/kg. At the ultra-high power density of 12000 W/kg, the energy density remains at 9.3 W·h/kg. Table S2 shows that these performances are better than that of reported MnO<sub>2</sub>-based energy storage devices. Figure S16(f) shows the

Nyquist diagram of ASC and the corresponding fitting results. The results show that the  $R_{ct}$  of ASC is  $1.3 \Omega$  and the equivalent series resistance ( $R_{es}$ ) is  $1.5 \Omega$ . Low resistance values indicate that ASC has excellent electrical conductivity. Figure S13 shows that the capacitance control contribution rate of ASC is significantly higher than that of  $MnO_2$ -3, and the Bode diagram of Figure S14 shows that ASC is closer to  $90^\circ$  than  $MnO_2$ -3, because the energy storage process of AC in ASC is significantly different from that of  $MnO_2$ -3. AC is a typical electric double-layer capacitor behavior, and  $MnO_2$ -3 and AC have synergistic effects. Figure S16(g) shows that when the current density is 3 A/g, the specific capacitance of ASC only decreases by 10% after 20000 cycles, indicating that ASC has excellent stability. In the initial phase of the cycle test, some fluctuations occurred in the curve, which is due to the continuous redox reaction between the electrode material and the electrolyte, the electrode structure will continue to dissolve and transform, and then stabilize. Figure S15 shows the electrochemical characterization of ASC after cyclic stability testing. After the cycle test, the shape of CV and GCD curves changed only slightly, and the EIS test showed that the  $R_{ct}$  and  $R_{es}$  were significantly reduced, which further indicated that ASC had excellent cycle stability. The illustration in Figure S16(g) shows that two ASCs in series can light a light-emitting diode (LED) lamp, proving that ASCs have good application prospects.

**Table S2** Comparison of electrochemical properties between this work and previously reported  $MnO_2$ -based materials

$MnO_2$ -based ASC	$E_{max}/(W \cdot h \cdot kg^{-1})$	$P/(W \cdot kg^{-1})$	Ref.
WC@ $MnO_2$ -20	12.2	22.3	[1]
$MnO_2$ @PC-0.06	13.6	250	[1]
$MnO_2$ /CNF/Ag-0.5	16.3	400	[3]
MXene// $MnO_2$	6.4	1170.7	[4]
AC// $MnO_2$ @ $NH_4MnF_3$	11.2	10000	[5]
$MnO_2$ -Cu//rGO	5.55	249.75	[6]
AC// $MnO_2$	15.84	885	[7]
$Fe_3O_4$ @ $MnO_2$ -HNS//AC	18.54	803	[8]
Lignin/ $MnO_2$ //AC	6	355	[9]
g-CN@ $MnO_2$ //PCNFs	1.6	84	[10]
$MnO_2$ -3//AC	18.4	400	This work

## References

- [1] ZHANG Xin-hao, LIU Xiao-yang, LI Ben-xian, et al. Rapid microwave synthesis of  $\delta$ - $MnO_2$  microspheres and their electrochemical property [J]. *Journal of Materials Science: Materials in Electronics*, 2013, 24(7): 2189–2196. DOI: 10.1007/s10854-013-1078-5.
- [2] TIAN Wen-hui, REN Peng-gang, HOU Xin, et al.  $MnO_2$  porous carbon composite from cellulose enabling high gravimetric/volumetric performance for supercapacitor [J]. *International Journal of Biological Macromolecules*, 2024, 261: 129977. DOI: 10.1016/j.ijbiomac.2024.129977.
- [3] SUN Rui, CHEN Ya, GAO Xuan, et al. Sodium lignosulfonate-derived hierarchical porous carbon electrode materials for supercapacitor applications [J]. *Journal of Energy Storage*, 2024, 91: 112025. DOI: 10.1016/j.est.2024.112025.
- [4] WEI Yu-di, ZHENG Ming-ming, LUO Wen-long, et al. All pseudocapacitive MXene- $MnO_2$  flexible asymmetric supercapacitor [J]. *Journal of Energy Storage*, 2022, 45: 103715. DOI: 10.1016/j.est.2021.103715.
- [5] LI Bin, ZHANG Xi-hua, DOU Jin-he, et al. Construction of  $MnO_2$ @ $NH_4MnF_3$  core-shell nanorods for asymmetric supercapacitor [J]. *Electrochimica Acta*, 2020, 347: 136257. DOI: 10.1016/j.electacta.2020.136257.
- [6] KUMAR A, THOMAS A, GUPTA A, et al. Facile synthesis of  $MnO_2$ -Cu composite electrode for high performance supercapacitor [J]. *Journal of Energy Storage*, 2021, 42: 103100. DOI: 10.1016/j.est.2021.103100.
- [7] LIAN Li-fang, YANG Jie, XIONG Pei-xun, et al. Facile synthesis of hierarchical  $MnO_2$  sub-microspheres composed of nanosheets and their application for supercapacitors [J]. *RSC Advances*, 2014, 4(77): 40753–40757. DOI: 10.1039/c4ra07880b.
- [8] TU Cheng-yu, LI Xuan, LU Cong-cong, et al. A sequential process to synthesize  $Fe_3O_4$ @ $MnO_2$  hollow nanospheres for high performance supercapacitors [J]. *Materials Chemistry Frontiers*, 2022, 6(14): 1938–1947. DOI: 10.1039/d2qm00450j.
- [9] JHA S, MEHTA S, CHEN Yan, et al. Design and synthesis of high performance flexible and green supercapacitors made of manganese-dioxide-decorated alkali lignin [J]. *Energy Storage*, 2020, 2(5): e184. DOI: 10.1002/est.2184.
- [10] SHIN M, SHARMA K P, KIM K, et al. The morphology and phase conversion of  $MnO_2$  in g-CN@ $MnO_2$  composite with supercapacitor applications [J]. *Journal of Physics and Chemistry of Solids*, 2023, 177: 111310. DOI: 10.1016/j.jpcs.2023.111310.